ADVANCED ENGINEERING MATERIALS
www.aem-journal.com

Mechanisms of De-icing by Surface Rayleigh and Plate Lamb Acoustic Waves

Shilpi Pandey, Jaime del Moral,* Stefan Jacob, Laura Montes, Jorge Gil-Rostra, Alejandro Frechilla, Atefeh Karimzadeh, Victor J. Rico, Raul Kanter, Niklas Kandelin, Carmen López-Santos, Heli Koivuluoto, Luis Angurel, Andreas Winkler,* Ana Borrás, and Agustin R. González-Elipe*

Acoustic waves (AW) have recently emerged as an energy-efficient ice-removal procedure compatible with functional and industrial-relevant substrates. However, critical aspects at fundamental and experimental levels have yet to be disclosed to optimize their operational conditions. Identifying the processes and mechanisms by which different types of AWs induce de-icing are some of these issues. Herein, using model $LiNbO_3$ systems and two types of interdigitated transducers, the e-icing and anti-icing efficiencies and mechanisms driven by Rayleigh surface acoustic waves (R-SAW) and Lamb waves with 120 and 510 µm wavelengths, respectively, are analyzed. Through the experimental analysis of de-icing and active anti-icing processes and the finite element simulation of the AW generation, propagation, and interaction with small ice aggregates, it is disclosed that Lamb waves are more favorable than R-SAWs to induce de-icing and/or prevent the freezing of small ice droplets. Prospects for applications of this study are supported by proof of concept experiments, including de-icing in an icing wind tunnel, demonstrating that Lamb waves can efficiently remove ice layers covering large LN substrates. Results indicate that the de-icing mechanism may differ for Lamb waves or R-SAWs and that the wavelength must be considered as an important parameter for controlling the efficiency.

1. Introduction

Ice accretion on materials operating outdoors or in sub-zero environments is a critical issue that significantly impacts efficiency, maintenance, and security in various industries, including aviation, energy generation, and the functionality of sensor and camera windows and screens. To address this problem, two primary approaches have been proposed: 1) Passive anti-icing based on applying surface engineering processes to reduce or delay ice accretion;[1–5] very often, these approaches rely on superhydrophobic or liquid-infused surfaces.[6–9] 2) Active de-icing/anti-icing systems applying different strategies for ice removal or preventing its formation; recent advances in the field include nanotechnology-based melting by Joule heating,[10] using materials such as graphene,[11–13] or photothermal de-icing using plasmonic or magnetic nanoparticles.[14–18] An emergent de-icing approach involves the activation of surfaces by high-frequency acoustic waves (AW) with

S. Pandey,[+] S. Jacob, A. Karimzadeh, A. Winkler
Leibniz IFW Dresden, SAWLab Saxony
Institute for Emerging Electronic Technologies (IET), Group "Acoustic Microsystems"
Helmholtzstr. 20, 01069 Dresden, Germany
E-mail: shilpi.pandey@tum.de; a.winkler@ifw-dresden.de

The ORCID identification number(s) for the author(s) of this article can be found under https://doi.org/10.1002/adem.202401820.

[+]Present address: Materials Science and Environmental Engineering, Faculty of Engineering and Natural Sciences, Tampere University, 589, 33104 Tampere, Finland

[Correction added on 17 December 2024, after first online publication: The 9th author name has been corrected in this version.]

DOI: 10.1002/adem.202401820

S. Pandey,
Heinz-Nixdorf-Chair of Biomedical Electronics
School of Computation, Information and Technology
Technical University of Munich
TranslaTUM, 80333 Munich, Germany

J. del Moral, L. Montes, J. Gil-Rostra, V. J. Rico, C. López-Santos, A. Borrás, A. R. González-Elipe
Nanotechnology on Surfaces and Plasma Lab
Materials Science Institute of Seville
Consejo Superior de Investigaciones Científicas (CSIC)
Americo Vespucio 49, 41092 Sevilla, Spain
E-mail: jaime.delmoral@icmse.csic.es

S. Jacob
German National Metrology Institute (PTB)
Bundesallee 100, 38106 Braunschweig, Germany

A. Frechilla, L. Angurel
Instituto de Nanociencia y Materiales de Aragón (INMA)
CSIC-Universidad de Zaragoza
50018 Zaragoza, Spain

nano-scale amplitudes, a procedure compatible with industrial-relevant surfaces. In this context, a key distinction should be made between the localized application to surfaces of commercially available ultrasound generators[19,20] and the innovative concepts based on the incorporation of piezoelectric active supports or layers, as well as electrodes (lateral field excitation (LFE) or interdigitated transducers (IDTs)), as integral parts of the surface to be activated.[21–26] The present work fits within this second approach, dealing with the integration of surface or bulk acoustic waves (SAWs and BAWs) for de-icing and ice sensing. Among the articles addressing this topic, the work of Yang et al. (2021), which proposes a strategy to weaken ice adhesion using Rayleigh surface acoustic waves (R-SAW),[21] is particularly noteworthy. For this purpose, IDTs with different wavelengths (100, 200, 300, and 400 μm) were manufactured on a 5 μm thick ZnO piezoelectric thin film deposited on an aluminum substrate, producing SAWs with frequencies comprised between 7.38 and 27.84 MHz. The authors state that SAWs produce vibrations comparable to "nano-scale earthquakes", which result in the generation of acoustic-heating effects, the development of micro-cracks, and the disturbance of ice nucleation through local vibrations and energy streaming into the formed liquid phase. The contribution of Joule heating effects directly stemming from ohmic losses in the IDTs cannot be discarded in these experiments since ice droplets were placed directly atop the IDTs. The same authors have recently claimed the possibility of monitoring ice formation using this type of SAWs.[22] Similarly, Zeng et al.[23] demonstrated a decrease in adhesion between ice and substrate due to interface heating and a reduction in electrostatic forces and mechanical interlocking on SAW-activated substrates. Del Moral et al.[24] and Jacob et al.[25] have recently extended the application of acoustic wave de-icing to transparent substrates and supports. In the first work, the authors demonstrated that extended electrodes on piezoelectric plates in an LFE configuration generate thickness shear mode - bulk acoustic waves (TSM - BAWs) in the 3–4 MHz range. These waves efficiently induced de-icing and a reduction of ice accretion (i.e., active-anti-icing effect), as well as a decrease in ice adhesion. A drawback of this approach is the necessity of a fast-electronic tuning of the excitation due to the very narrow bandwidth of BAW modes. The possibility of using the same device for ice detection under realistic operation conditions (i.e., experiments in icing wind tunnels (IWT)) and a profitable synergy to reduce power consumption upon the application of anti-icing coatings were also demonstrated in Del Moral et al. work.[24] On the contrary, Jacob et al.[25] demonstrated that R-SAW technology can be applied to large areas and transparent substrates beyond the centimeter scale, proving that R-SAWs can be used for de-icing industrially relevant surfaces. In that work, the authors also demonstrated that R-SAWs generated on piezoelectric plates and piezoelectric thin films induced the de-icing of glaze ice through a pure acoustic mechanism, discarding the melting through direct electrothermal (Joule) heating induced by ohmic losses in the IDTs on substrates with low thermal conductivity. Recently, the same authors demonstrated that a hybrid operational mode is possible by combining R-SAW for de-icing and BAW for sensing by carefully controlling the excitation mode of the two finger combs integrated into the IDTs.[26] Other relevant studies on the implementation of AW ice sensors and de-icing of rime ice have also been recently published.[27–30]

Despite the significance of these contributions, de-icing with substrate-integrated AW systems faces substantial fundamental uncertainties that still hinder the implementation of this technology in real-world applications. Critical bottlenecks encompass the assessment of factors affecting the transmission of AW energy to ice or water present on the device surface, understanding the mechanisms behind ice-cracking and other processes contributing to ice removal without complete melting, and defining activation conditions to avoid ice formation under subzero temperatures, thereby enabling an efficient anti-icing mode. Additional features preventing an unequivocal comparison of efficiencies and de-icing mechanisms are the differences in the type of AWs, either SAWs, Lamb waves, or TSM-BAWs,[21–26] the effect of the substrate materials (e.g., transparent and black LN, ZnO thin films deposited on different substrates such as Al foils, glass and fused silica, the hydrophobic or hydrophilic surface modification of these substrates, etc.), or the plethora of conditions used in the experiments (type of ice, liquid water content (LWC) when working in IWTs, static and windy conditions, temperatures and relative humidity, water freezing or ice accretion, etc.).

To shed some light on this twilight scenario, we herein systematically investigate the de-icing and active anti-icing activation of the same substrate with either R- SAW or Lamb waves. For this purpose, we use $LiNbO_3$ (LN) piezoelectric chips activated with IDTs operating at different driving frequencies. The selection of LN for preparing specific model systems to study de-icing with AWs exceeds this topic, as this piezoelectric material is widely utilized in other applications such as high-temperature sensors or optical waveguide tapered antennas.[31–33] Herein, we have electro-acoustically characterized a series of IDT configurations to optimize their performance, either for activating R-SAWs or Lamb waves. Then, for these two wave modes and various subzero temperatures, we performed de-icing and active anti-icing experiments of small ice aggregates and water droplets, monitoring the threshold power required in each case. Additionally, an analysis of the operational conditions of the chips using finite element model (FEM) simulations in COMSOL Multiphysics is used to model the generation of the R-SAW and Lamb wave modes and account for their interaction with ice. Finally, to validate these experimental and simulation results for Lamb waves, we have carried out some proof-of-concept de-icing experiments proving the suitability of the Lamb wave activation to remove large areas of accreted ice. The overall assessment of the de-icing of small ice aggregates and large ice layers with Lamb waves has permitted the proposal of a specific mechanism of de-icing using Lamb waves that differs from that already known for R-SAWs.[25,30] We are confident that all these findings will significantly contribute to establishing a rational pathway for exploiting AWs as the basis for a next-generation de-icing system.

R. Kanter, N. Kandelin, H. Koivuluoto
Materials Science and Environmental Engineering
Faculty of Engineering and Natural Sciences
Tampere University
589, 33104 Tampere, Finland

2. Experimental Section

2.1. Fabrication and Electroacoustic Characterization of AW Chip Devices

The selected piezoelectric material was a 0.5 mm thick black Lithium Niobate 128° YX wafer cut purchased from CSIMC-Freqcontrol, China. The 4 inch wafers were cleaned with acetone and IPA using ultrasonic cleaning for 5 min and O_2 plasma treatment at 100 W for 10 min. IDTs were patterned using photoresist spin-coating, a maskless laser writer (Heidelberg instruments MLA 100), and the lift-off technique. Ti (5 nm)/Al (295 nm) was selected for IDT metallization. Further, 100 nm SiO_2,[34] was deposited by magnetron sputtering on top of the wafer. This layer acts as a passivation layer and protects the aluminum IDTs from corrosion. This SiO_2 thin film confers a hydrophilic character to the surface of prepared chips (wetting contact angle ≈35°). The contact pads were opened for electrical contact by a dry etching procedure. Figure S1 in the Supporting Information section (SI) shows the utilized mask design and a manufactured wafer aimed at fabricating IDTs with wavelengths varying from 120 to 510 μm and an aperture of 9.95 mm, including various designs with a different number of finger pairs. Chips operating at different wavelengths were diced into individual chips, as shown in Figure S2, Supporting Information. Keeping the same apertures and number of finger pairs, different IDTs layouts and sizes of diced LN plates were used for the chips utilized for proof-of-concept experiments, as explained in the corresponding section. Chip sizes of 15 × 20, 15 × 25, and 15 × 30 mm^2 have been prepared on the wafer, depending on wavelength. The devices with 120 and 510 μm wavelength (henceforth called 120 chip and 510 chip, respectively), used for the de-icing experiments of small ice aggregates as done in this work, were prepared on 15 × 20 and 15 × 30 mm^2 LN pieces, respectively. A 420 μm chip was also prepared for a comparative de-icing test with big ice aggregates. This ensured a minimum area of 15 × 10 mm^2 without IDTs for de-icing experiments.

For the electroacoustic characterization of the chips as a function of finger pairs, on-wafer electrical measurements were carried out using a vector network analyzer (VNA, Keysight E5080B) and a wafer prober (Figure S3, Supporting Information). Before RF measurement, a viscous photoresist was applied between the IDTs to attenuate the waves and neglect reflections on neighboring IDTs, thus avoiding undesired effects by measuring the reflection coefficient (S_{11}) curves.

2.2. De-icing and Active Anti-icing Tests with Small Ice Aggregates

De-icing and anti-icing experiments were carried out in a custom-made icing chamber, where temperatures down to a minimum value of −20 °C can be controlled (see Figure S4, Supporting Information, showcasing a view of this chamber, the chip holder, and the water dosing system). An ad-hoc water dosing system consisting of heatable tubing inserted via the wall of the cooling chamber was employed to enable the dosing of droplets of bi-distilled water on the surface of the chips to produce ice particles. Inside the chamber, the tube was kept at a temperature of 2 °C to prevent water freezing inside the tube. The temperature of the substrate was controlled independently from that of the cooling chamber by a Peltier plate on which the holder and printed circuit board (PCB) were placed. Several thermocouples were mounted on the stage and the droplet hose to precisely control the temperature of the chip and water droplet dispenser. A USB camera with an attached C-mount objective was placed out of the cooling chamber to follow the evolution of ice aggregates and droplets.

De-icing and active anti-icing experiments were conducted on chips with IDTs of 120 and 510 μm in this custom-built cooling chamber. The icing tests were performed with the best-suited configuration of available chips (according to the number of finger pairs) as determined by their electro-acoustical characterization.

Experiments were carried out at three temperatures (−5, −10, and −15 °C, as controlled on the Peltier plate) with the stage in a horizontal position. At these temperatures, the porosity and nature of ice formed upon accretion processes from the impact of supercooled water droplets change from glaze (at −5 °C) to mix (at −10 °C) to rime (at −15 °C).[35] However, under the experimental conditions of herein-reported experiments, the ice did not form by accretion but by cooling sessile water droplets. These conditions are prompt to generate little porosity. The stage temperature was continuously monitored during the experiments using a thermocouple mounted on an aluminum holder in direct contact with the Peltier plate. Once the temperature was stabilized, a 22 μL milliQ water droplet at +2 °C was dispensed on the surface of the chips at a distance of ≈3 mm from the IDTs. After a while, the dispensed water droplet froze into a small aggregate of ice, and then the chip was electrically excited until the ice was completely melted. The minimum activation power (we denote this de-icing power as DP_T, a magnitude that depends on temperature T) has been taken as a relevant parameter for comparing the de-icing efficiency of the 120 and 510 μm chips. For the active anti-icing experiments, the same volume of water was dripped on an electro-acoustically activated chip, and the minimum power required to prevent freezing (anti-icing power, AP_T) was taken as the relevant parameter for comparing efficiencies. In these experiments, the surface was permanently activated to avoid ice nucleation and the subsequent freezing of the deposited water droplet.

The RF AW activation of the chips inside this cooling chamber was done by contacting the diced chips via a 50 Ω impedance PCB provided with gold-coated spring-pin connectors as shown in Figure S2, Supporting Information together with the chip holder adapted to conduct the de-icing experiment. An RF supply, BSG F20 (BelektroniG GmbH, Germany), has been used for electroacoustic excitation, and the power supplied by the instrument has been taken as a reference parameter of the actual applied power.

2.3. Proof of Concept: Experiments for De-icing Large Ice Layers with Lamb Waves

Two proof-of-concept experiments using Lamb waves have been carried out to determine the de-icing mechanisms of this type of wave applied to large-area ice layers or aggregates.

2.3.1. Experiment 1

In the 510 μm chip used for this experiment, the IDT and connection pads were structured on the LN face that was not exposed to ice accretion. This means the 510 μm IDTs and PCB board were on the opposite side of the ice-formation surface. The connecting board was adequately protected to prevent shortage or malfunction with the IDT layout in the center of the LN plate and the connecting pads at each side of the chip (Figure S5, Supporting Information shows the chip, PCB, and protecting board). In this configuration, the connecting pad at the top side of the chip was the electrically polarized one, while that at the bottom was grounded. The icing area was equivalent to the $15 \times 30\ mm^2$ chip size. Ice accretion was done in the IWT facility available at the TAU laboratory (detailed information about these Ice Laboratory facilities can be found in Koivuluoto et al.[36]). A maximum wind speed of $25\ m\ s^{-1}$, with a liquid water content of $0.5\ g\ m^{-3}$ at a temperature of −10 °C was used to accrete the ice in this experiment. The formation of a mixed ice type is expected from these experimental conditions. An ice film with a thickness between 0.5 and 1 mm, depending on the location on the chip surface, was accreted and kept in the wind tunnel chamber at −10 °C before being subjected to AW activation.

2.3.2. Experiment 2

The experiment was performed with a 510 μm chip of $15 \times 30\ mm^2$ with the IDT structured on the ice-exposed side of the LN plate. In this case, a larger volume of water of ≈180 μL was deposited in ambient air on the chip surface outside the zone of IDTs. The water covered an area of $\approx 0.9\ cm^2$, separated by a distance of ≈2 mm from the IDT. Then, the chip and connecting board were placed inside the cooling chamber, and the temperature decreased up to −15 °C to induce rime ice formation. Afterward, the chip and board were removed from the cooling chamber, and the AW de-icing was induced in ambient conditions immediately after connecting with the electronics (total time shorter than 10 s). The process was followed by placing a video camera outside. During this time, the sample temperature never surpassed 0 °C without AW activation. These conditions generated some frost on top of the surface of the chip due to water vapor condensation, as visible during the experiments. For comparative purposes, a similar experiment to the one done in Experiment 2 was also carried out with a 420 μm chip generating Rayleigh SAWs.

For the experiments, the electronic control and activation systems were placed outside either the cooling chamber (experiment 2) or IWT (experiment 1, although in this case, the ambient temperature was −10 °C). Electronics consisted of a vector network analyzer (VNA) to determine the working frequency during and after ice accretion and a switch allowing to automatically connect the chip to a signal generator system consisting of a signal generator (Keysight33210A) and an amplifier (Mini-Circuits LZY-22+). Further details of this electronic control and activation system can be found in Del Moral et al.[24] The reported de-icing experiments were carried out applying an RF signal at around 7.3 MHz with slight variations in the order tenths of kHz depending on the chip and peak-to-peak voltages of 53 V (experiment 1) and 70 V (experiment 2), equivalent to approximate power values of 1.7 and 4.8 W, respectively.

2.4. Finite Element Model (FEM) Calculations

Finite element (FE) simulation of the 120 and 510 μm chips was conducted using COMSOL Multiphysics version 6.0. This simulation describes the generation and propagation of AWs and their interaction with ice, verifying the easiness of mechanical energy transmission through the piezoelectric LN and the ice interface. For this purpose, we have calculated the displacement field (u) in the substrate and the ice aggregate under the assumption that larger displacements in the ice aggregate mean a better transmission of the mechanical energy of the AW from the activated LN to ice. The ice aggregate was located at the same distance from the edge of the last finger of the IDT as in the experiments, trying to reproduce their actual conditions. To keep the computational costs within reasonable limits, the volume of the simulated droplet has been settled at 4 μL. Ice aggregates were assumed to present a hemispherical shape, as it typically happens after freezing water droplets deposited on surfaces.

The AW vibrations of the LN plate with IDTs have been modeled using a series of electrodynamic and mechanic equations, as previously described by Fakhfouri et al.[37] Since R-SAW and Lamb waves on 128° X–Y $LiNbO_3$ are mainly polarized in the median plane,[38] a two-dimensional (2D) model was simulated using a generalized plane strain assumption. This assumption has been adopted to simulate both the 120 and 510 μm chips. The 0.5 mm thick substrate has been described with the elasticity, piezoelectric, and electric permittivity tensors of LN,[39] which were adequately rotated to account for the actual 128° X–Y crystal cut of the substrates used in the experiments. The ice was modeled as an isotropic linear-elastic material in the form of a semicircle geometry, using the ice properties provided by Victor and Whitworth,[40] corresponding to a compact type of ice similar to glaze ice. All this information, including the description of the characteristics of the IDTs, dimensions, applied voltage, time step used for the simulations and dimension, and other computational parameters, can be found in the SI section, SI6. Notably, the ice–substrate interface between the ice and the LN substrate has been simulated as flat, an assumption that fits well with the conditions of the real system formed by a single crystalline substrate with very little surface roughness. An ideal system consisting of an R-SAW with a long wavelength (510 μm) interacting with the ice aggregate was also simulated for comparative and discussion purposes. The parameters used for computing the 510 μm Lamb wave system were kept for this ideal system, except for the assumption of a finite thickness for the LN substrate. This semi-infinite thickness boundary condition reduces reflection of the AW at the bottom face of the plate to a minimum, that is, imposing a situation typical of the generation of R-SAWs. This simulated model will be designated in the text as 510 μm R-SAW to differentiate it from the simulated model for the 510 μm Lamb waves.

Figure 1 presents a scheme with the definition of system coordinates (x, y, z) used for calculations. Since the COMSOL Multiphysics calculations have been carried out in two dimensions (2D), the relevant coordinates are x and z (c.f. Figure 1b).

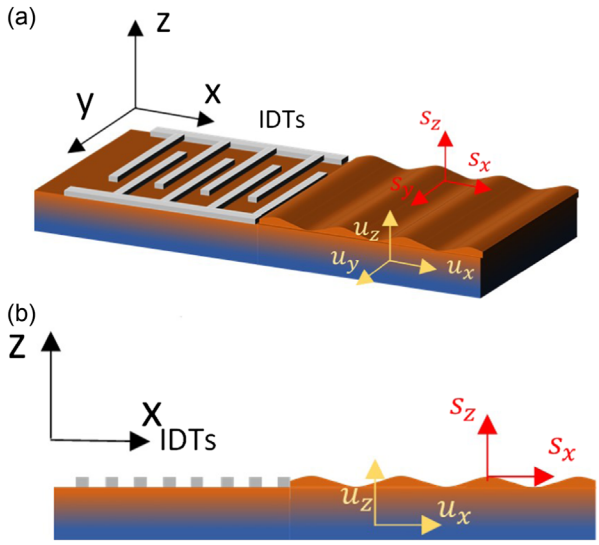

Figure 1. Schematic description of the geometry of chips with displacement field and axis definitions; a) 3D diagram of the chip; b) 2D diagram of the chips as used for the calculations.

The former corresponds to the propagation direction of the wave, while the latter corresponds to the perpendicular to the LN plate.

For calculations, figures, and data presentation, we have adopted the following definitions: 1) Volumetric displacements: the local, wave-induced displacement field undergone by the lattice of the LN plates. They are characterized by a lattice displacement vector **u**. The relevant magnitudes for data calculation and presentation are its modulus in 2D $|\mathbf{u}|$ and the two components u_x and u_z. 2) Surface displacements: the displacement field undergone by the outer surface of the plate, which in the icing experiment is in contact with the ice and is directly involved in the transmission of the mechanical energy to the ice. This definition simplifies the notation and remarks on the importance of power confinement on the surface of the chip. Surface displacements are characterized by a surface displacement vector, **s**. The relevant magnitudes to present data and for calculations are its modulus in 2D $|\mathbf{s}|$ and the two components s_x and s_z.

The geometry of the whole system has been discretized with an unstructured triangular mesh, and the acoustic modes have been described with at least 10 elements per wavelength considering the following sound velocities: in LN substrate 3981 m s^{-1},[39] in ice 1850 m s^{-1}.[40] The resulting grid had approximately three million elements (equivalent to ≈18.3 million degrees of freedom). Electrical excitation was modeled using an electric potential that follows the periodicity of the IDT fingers, which were located on the left half of the model geometry, neglecting the mechanical damping of the metal electrodes. To avoid undesired reflections of the AWs at the edges of the chips, the AWs were absorbed by incorporating perfectly matched layers (PML) as defined in the COMSOL software documentation.[41]

The model was solved in both the frequency domain and the time domain using a frequency solver or a time-dependent solver, respectively. In the frequency domain, the IDTs were defined as an RF port where power is explicitly defined as an input parameter (1 W was arbitrarily selected for the calculations since simulations are linear and provide S_{11} spectra and harmonic solutions of the displacement and electric fields, no dependence of results is expected on the used input power). Simulations were also done in the time domain to obtain real-time estimation of the vibroacoustic response of the LN plate and the LN/ice systems upon electroacoustic excitation. In this case, the electrical excitation is applied to the IDTs as a sinusoidal voltage signal with defined amplitude and working frequency as input parameters. Working frequencies were selected based on the frequency domain results following maximum power transmission criteria. To generate equivalent mechanical powers for the AWs in the simulation of the 120 and 510 µm chips, the selected voltage amplitudes in each case were different to compensate for the differences in electroacoustic coupling. Therefore, the resulting electric power for each wavelength was slightly different to ensure that the generated mechanical power was equivalent in all simulated models.

3. Results and Discussion

3.1. RF Characterization of AW Chips

The radio-frequency (RF) electrical characterization of the chips was performed by measuring the S_{11} (return loss) and $|S_{11}|^2$ (reflection coefficient of power) parameters as a function of frequency. The measured resonance frequencies (frequency of the S_{11} minima) closely match the calculated resonance frequencies of the chips, according to the well-known expression

$$f = \frac{v_s}{\lambda} \tag{1}$$

where f, v_s, and λ are, respectively, the working frequency, the wave velocity on 128° YX LN substrate (3981 m s^{-1})[39] and the wavelength, this latter defined by the IDT layout (i.e., the distance between fingers). The series of return loss spectra plotted as a function of frequency recorded for the different chips prepared in this work are reported as SI7. These spectra show that the S_{11} minima deepen for a higher number of finger pairs. To minimize the reflected power, de-icing tests were carried out with 120 and 510 µm chips with the largest number of finger pairs tested during the electroacoustic evaluation, that is, 15 and 26, respectively.

To estimate the power efficiency, the reflection coefficient of power $|S_{11}|^2$ is the relevant parameter, which can be calculated from Equation (2) and (3):

$$\mathrm{RL(dB)} = 10\log_{10}\left(\frac{P_i}{P_r}\right) \tag{2}$$

$$|S_{11}|^2 = \frac{P_r}{P_i} \tag{3}$$

where RL(dB) is the return loss of the chips and P_r and P_i are reflected and incident power, respectively.

Figure 2 shows a series of plots of the reflection coefficient of power $|S_{11}|^2$ versus frequency as recorded for the 120 and 510 µm chips with different numbers of finger pairs. A photograph of these two chips is also included in the figure. The full set of

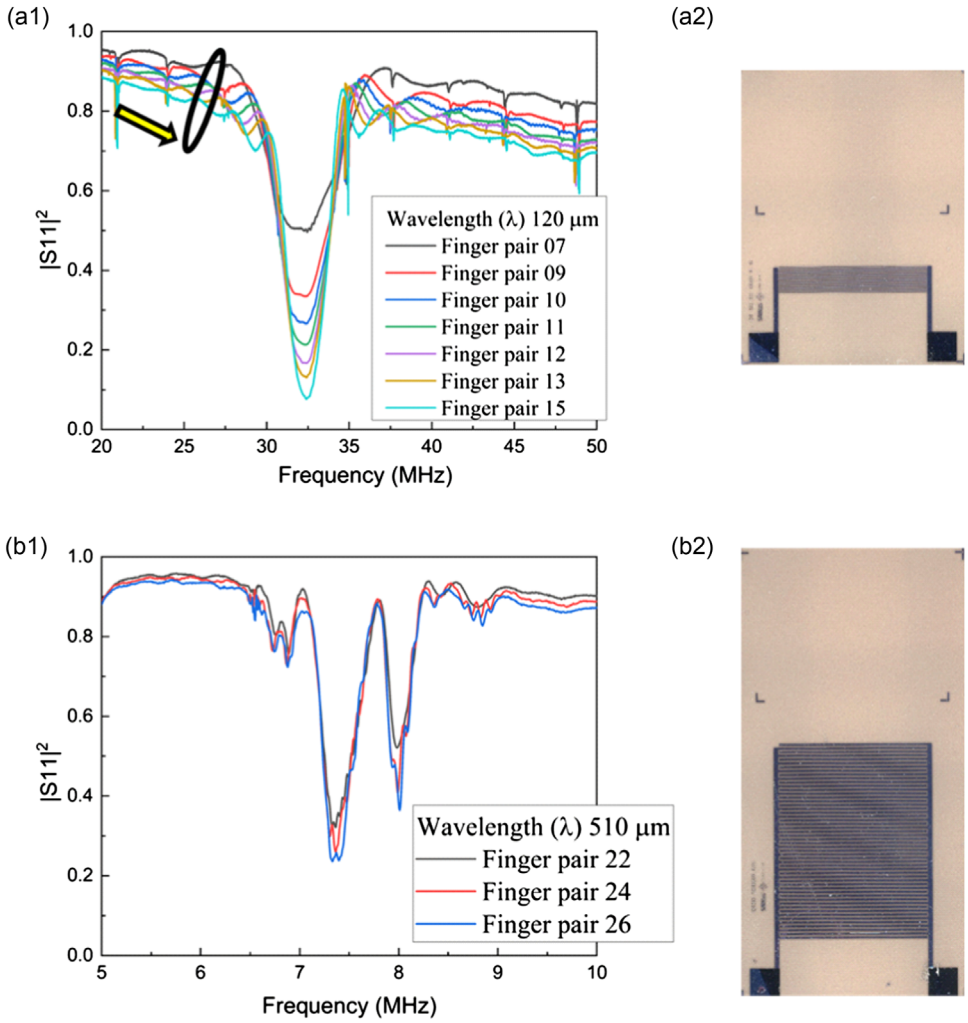

Figure 2. Electrical characterization of AW chips: a1,b1) $|S_{11}|^2$ versus frequency plots for fabricated AW devices with wavelengths (λ) of 120 µm (a1) and 510 µm (b1). Note the different span of the *x* scales used in each case. The arrow and ellipse highlight the progressive increase of power losses in the series of 120 µm devices as the number of finger pairs increases. Photographs of the 120 µm a2) and 510 µm b2) chip devices with the maximum number of finger pairs.

$|S_{11}|^2$ curves recorded for all manufactured chips is shown in Figure S7, Supporting Information.

To ensure the maximum efficiency of the devices, they should present $|S_{11}|^2$ values close to zero to minimize the reflected power upon electrical activation. The plots in Figure 2 show that the reflected power is highly dependent on the number of finger pairs and decreases when its number increases. For the longest wavelength chip, that is, the 510 µm chip, power losses reached saturation at $|S_{11}|^2$ values around 0.25 for 26 finger pairs. For the 120 µm chip, a $|S_{11}|^2$ value smaller than 0.1 is reached with 15 finger pairs. In general, although the reflection coefficient of power could still slightly decrease by increasing the number of finger pairs, the benefits would be very small and likely compensated by the electrical power losses that also increase with this parameter. Therefore, we have selected 15 and 26 finger pairs for the 120 and 510 µm chips for de-icing and anti-icing experiments. This choice is a good compromise between low reflection and an acceptable free chip area for de-icing experiments (see below).

These plots in Figure 2 also reveal a lowering in baseline for the 120 µm chip (ideally, $|S_{11}|^2$ should equal one outside of the resonance peak), which is particularly noticeable for the 120 µm chip. This indicates the existence of some electrical power losses, which are not due to the resonance excitation of the crystal and are likely caused by factors such as parasitic capacitances in the IDT, ohmic resistance of the thin film metallization, or contact resistances. These parasitic losses are in the order of 10–20% for the characterized chips, a percentage of the incident power that will not contribute to the generation of AW vibrations through electromechanical coupling. The plots in Figure 2 also show that, as expected, these electrical power losses increase with the number of finger pairs.

According to Figure 2, S7/S8, Supporting Information, the electroacoustic response of the 510 µm chip is different. The behavior of this chip is characterized by two resonance minima instead of one in the frequency region of interest. We attribute these two resonances to Lamb plate waves instead of Rayleigh

waves. According to the well-established theory of SAW generation in piezoelectric plates,[42] an R-SAW can be regarded as the high-frequency limit of the superposition of symmetric and antisymmetric Lamb waves. These two counterparts start to separate for plate thicknesses of around 1.5 λ. From the $|S_{11}|^2$ plots in Figure 2, it appears that when the wavelength of the AW approaches the thickness of the plate, the conditions for pure Rayleigh-SAW are no longer fulfilled. According to these considerations and Equation (1), the resonance at 7.36 MHz corresponds to the A0 Lamb wave mode, whereas the ≈8 MHz resonance must be attributed to the S0 Lamb wave mode. In the next section, we further support this attribution by the simulations obtained using COMSOL Multiphysics analysis of the AWs in the 510 μm chip. RF chips with a similar configuration but a wavelength larger than 510 μm behave similarly and generate two AWs at different frequencies (see Figure S8, Supporting Information for the $|S_{11}|^2$ curves experimentally determined for a 600 μm chip, which is reported for comparison).

Table 1 includes experimental and calculated (i.e., Equation (1)) resonance frequencies for the manufactured chips with the maximum number of finger pairs in each case, as well as the type of generated AW.

3.2. FEM Simulation of AW

Simulation results of the AW generation and propagation in the 120 and 510 μm chips were carried out as described in the Experimental and Methods section. **Figure 3**a,b present selected results of this simulation analysis for each type of wave. Videos (V1_S10) and (V2_S11) provided as SI showcase the time-dependent variation of volumetric displacements represented in the form of color maps with the same color code as for the snapshots in Figure 3a2,b2.

The plots in Figure 3a1,b1 compare the experimental and calculated $|S_{11}|^2$ spectra of the 120 and 510 μm chips. The concordance between curves obtained with experiments and simulations confirms that simulations reproduce the experimentally recorded signals, except for the electrical IDT power losses evidenced by the non-zero backgrounds of the experimental curves, a feature particularly noticeable for the 120 μm R-SAW. This proves that, except for this deviation attributable to ohmic losses and/or capacitive effects in the real chips not included in the analysis, the simulations for the two chips agree with their actual behavior.

The analysis in Figure 3a2 of the volumetric displacements determined in the time domain for the 120 μm chip confirms that vibrations only affect the outer surface layers of the LN plate, as expected for a typical R-SAW type (see video (V2_S11), Supporting Information). This is evidenced by the color maps in this figure showcasing snapshots of the modulus ($|\mathbf{u}|$) and u_x and u_z components of volumetric displacements of this wave that confirm the confinement in the outer surface regions of the plate. The plots in the same figure representing the value of $|\mathbf{u}|$ along the plate thickness as a function of the coordinate z show that the displacement field goes to zero in the bulk.

Figure 3a3 presents the plots of surface displacement components s_x, s_z, and the modulus of the displacement vector at the surface $|\mathbf{s}|$ along the direction of wave propagation (x). Notably, these parameters correspond to the AW-induced displacements in the plate outer plane of the chip plate, that is, the surface that will be in contact with the ice. Figure 3a3 reveals that maximum displacements along x and z are almost equivalent and are separated by a phase shift of 93°. This result means that the surface displacement field approaches a circular polarization, as shown by the plot in Figure 3c representing the component s_x versus s_z (note that the different circles in the plot refer to calculations at different times).

The "in the time domain" simulation of the electroacoustic activation of the 510 μm chip in Figure $3b_1$ gives rise to two well-defined and distinguishable $|S_{11}|^2$ peaks matching the shape of the experimental curves, as well as the frequency values of the minima (Table 1). Meanwhile, the analysis in Figure $3b_1$ demonstrates that volumetric displacements affect the whole plate thickness. The color plots in this figure show that the first peak at 7.4 MHz (note that there is a small difference with respect to the experimental minimum at 7.36 MHz) corresponds to vibrations with anti-symmetrical character and should be attributed to a A0 vibrational mode. Meanwhile, volumetric displacements corresponding to the second peak at 8.1 MHz have a symmetrical character (i.e., typical of an S0 mode, data not presented). Meanwhile, plots in this figure for $|\mathbf{u}|$ as a function of the coordinate z within the plate show that the displacement field does not vanish in its interior and extends from one face to the opposite of the LN plate. Figure $3b_3$ shows that the magnitude of s_x and s_z components is similar, and there is a phase shift of 91° between them, that is, the surface displacements are circularly polarized. This is confirmed by the representation of s_x versus s_z in Figure 3c.

When comparing the waves generated in the 120 and 510 μm chips, it is noteworthy that they present surface and plate character, respectively. Another significant difference is that the surface displacements in the 510 μm chip for the A0 mode are slightly smaller than for the 120 μm chip, and they present a certain modulation due to the superposition of a second contribution of much larger wavelength in the order of 4–5 mm. This second contribution is likely due to a weak standing wave mode with a larger wavelength that is superimposed on the main one (see Figure S9, Supporting Information).

Table 1. Calculated and experimental frequencies for the best IDT configuration of the chips in terms of the number of finger pairs.

Wavelength [μm]	Number of finger pair	Measured frequency [MHz]	Calculated frequency [MHz]	Mode
120	15	32.32	33.25	R-SAW
150	16	25.79	26.60	R-SAW
240	20	16.10	16.62	R-SAW
330	22	11.68	12.09	R-SAW
420	28	≈9.20	9.50	R-SAW
510	26	≈7.36 & 8.14	–	Lamb wave

3.3. De-icing Experiments of Small Ice Aggregates

To verify the effect of the AW characteristics on the de-icing process, we have systematically compared a series of de-icing experiments carried out with the 120 and 510 μm chips. According to the previous simulations in Section 3.2, these chips generate Rayleigh SAW and Lamb waves, respectively.

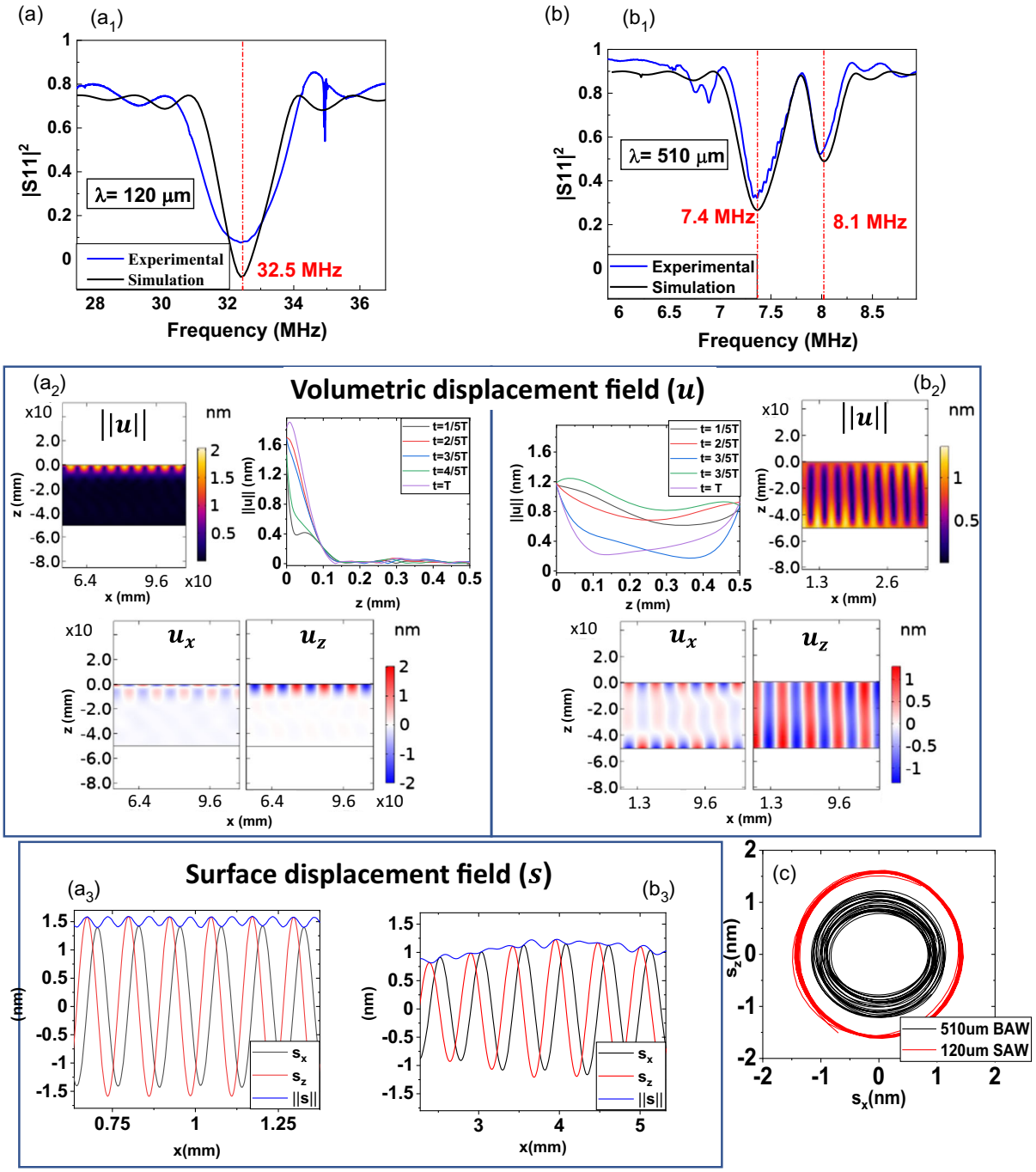

Figure 3. Simulation of the AWs: a,b) simulations for the for the 120 μm (a) and 510 μm (7.4 MHz peak) (b) chips. a_1,b_1) simulation in the frequency domain of $|S_{11}|^2$. a_2,b_2) simulation in the time domain of the bulk displacements. Simulations include: i) color maps snapshots of the bulk displacements (modulus |**u**| and u_x and u_z components); ii) plots at various times of the modulus of the bulk displacement vector |**u**| along the coordinate *z* (thickness of the plate). a_3,b_3) plots the modulus |**s**| and s_x and s_z components. Note that the *x* scale is not the same for the two waves to properly compare the displacement fields. c) Plot of the s_x versus s_z components to assess the polarization of the displacement field at the surface in the two chips.

Experiments were done at temperatures of −5, −10, and −15 °C. A summary of the experimental conditions is shown in **Table 2**, including information about temperature, actual frequency, and incident power values (i.e., DPT values), as well as an estimation of the effective power actually available for AW excitation. The latter have been estimated after the correction of the experimental DP_T values. A first correction considers that the electrical power that is not inserted into the LN plate in the form of AW electromechanical activation would be equivalent to 1- $|S_{11}|^2$. For instance, for the 120 μm chip with 15 finger pairs, it

Table 2. De-icing data for the 120 and 510 µm chips: temperature, operating frequencies, incident (DP_T), and effective AW powers after correction by the estimated losses.

Chip [µm]	Temperature [°C]	Frequency [MHz]	Incident power[a] (DP_T) [W] ± error	Effective power [W]
120	−15	32.33	3.76 ± 0.26	2.70
	−10	32.40	2.76 ± 0.68	1.98
	−5	32.44	1.46 ± 0.20	1.05
510	−15	7.36	2.02 ± 0.39	1.39
	−10	7.40	1.46 ± 0.29	1.00
	−5	7.36	1.45 ± 0.16	1.00

[a]The uncertainty limits for the DP_T values define the variation in the measurements in each case.

appeared that approximately an 8% of the incident electrical power is not efficiently coupled to the device. As indicated in Section 3.1, parasitic electrical power losses associated with the IDTs should be summed up in this correction. Parasitic losses were important for the 120 µm chip with 15 finger pairs, which amounted to ≈20% of incident power (c.f., Figure 2). In total, a rough estimate of the electrical power actually converted into mechanical excitation with this chip might be in the order of 72% of the incident power (this percentage stems upon substrating the 20% of parasitic losses plus ≈8% due to the coupling issues). For the 510 µm chip, a similar analysis gives an estimated correcting factor of 69% (note that in this case ohmic or capacitive losses associated to the IDTs were smaller, c.f. Figure 2). Since the estimated power losses resulting from these correcting factors were rather similar for the 120 and 510 µm chips, comparative assessments of powers and efficiencies would be equivalent using either incident or effective power values. Note, however, that heating effects due to ohmic losses at the IDTs will likely be higher for the 120 µm chip.

The de-icing experiments proceeded in the following way: once the chip temperature was stabilized in the cooling chamber, the system was kept under these conditions for at least 30 min for temperature homogenization. Then, a liquid droplet (+2 °C, 22 µL) was delivered and frozen on the surface of the chips, forming a hemispherical ice aggregate defined by a circular perimeter of ≈4.5 mm. Then, an RF signal with the incident (DP_T) power reported in Table 2 was applied to generate AWs at the resonance frequencies of each chip. The reported values correspond to the minimum incident power required to induce melting. Both DP_T and the effective AW power values in Table 2 confirm that melting on the 510 µm chip is more favorable than on the 120 µm chip. We tentatively attribute this difference to the distinct characteristics of the waves generated in each case, a feature that will be further discussed in the following sections.

The melting sequence induced upon application of the reported powers in Table 2 was video-recorded for both chips. **Figure 4** shows a series of snapshots representing dripping (Figure 4a1,b1), freezing (Figure 4a2,b2), partial melting

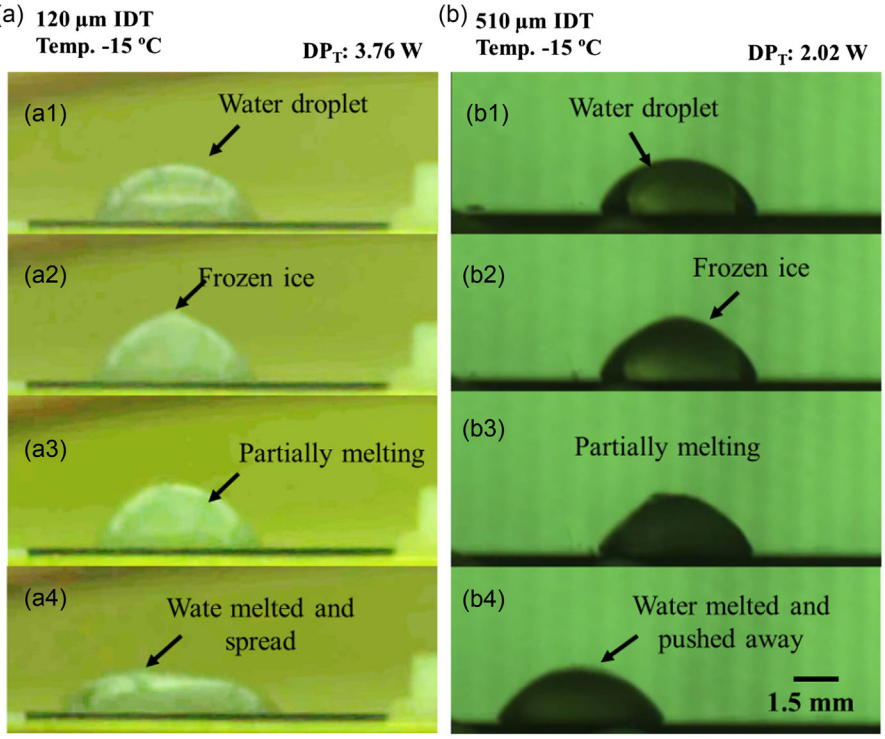

Figure 4. Comparison of de-icing process on the a) 120 µm and b) 510 µm chips. A 22 µL droplet is delivered on the chips at –15 °C a1,b1); droplet is frozen; a2,b2): droplet starts melting, after chip activation with the DP_T powers reported in Table 2 a3,b3); droplet remains liquid (active anti-icing effect) a4,b4). The behavior of the melted water droplet was different for the two chips: it spread for the 120 µm chip but was pushed toward the chip edge in the case of the 510 µm chip. The water droplet was dispensed at almost similar distance from the last finger of the IDTs (i.e., at about 3 mm).

(Figure 4a3,b3), and final melting (Figure 4a4,b4) stages of the experiments performed at −15 °C. Results of similar experiments at −5 and −10 °C are reported as SI section in Figure S10 in the SI section and the videos (V4_S15 and V5_S16), Supporting Information.

In general, longer times were required for de-icing with the 120 μm than the 510 μm chips. For example, at −5 °C only a slightly higher power of 1.46 W was required for de-icing with the 120 μm chip against 1.45 W for the 510 μm chip (c.f. Table 2). However, the droplet began to melt after ≈70 s of activation and completed the process after 170 s on the 510 μm chip. In contrast, it required 230 s to achieve complete melting with the 120 μm chip. A similar behavior was also observed at the other temperatures. Thus, at −15 °C, the power required to melt the ice aggregate was 3.76 W with the 120 μm chip and applied for a time longer than 215 s for completion. Remarkably, at this temperature, less power was needed with the 510 μm chip, for which an incident power of 2.02 W and an excitation time of 65 s was sufficient to achieve complete de-icing.

Additional differences were observed during the melting process and in the final melted states. In the intermediate states (i.e., stages a3 and b3 in Figure 4), the droplet shape became occasionally asymmetric on the 120 μm chip, while it remained always symmetric on the 510 μm chip. This occasional asymmetry might be a hint that melting has begun on the right side of the droplet, where liquid water would form due to the interaction with the traveling R-SAW moving from the right to the left in the images. Such a lateral melting mechanism has been previously discussed by us in Jacob et al.[25] dealing with R-SAWs. Meanwhile, the preservation of the symmetric shape of the droplets on the 510 μm chip suggests that melting is progressing through the whole ice-substrate interface with no lateral inhomogeneity in the water-ice distribution. Significantly, once the droplets are entirely melted (stages a4 and b4 in Figure 4), strong vibrations were visible inside the ice drop with the 510 μm chip, the droplets displacing further toward the edge of the chip. Water displacements have been amply reported in the literature for the AW excitation of water droplets.[43–45] The use of AW to induce de-fogging, removal of water droplets, or cleaning of surfaces has also been studied.[46,47] In the herein reported experiments (c.f. Figure 4 and S10, Supporting Information), water droplet displacements were not observed on the 120 μm chip. Thus, water droplets spread laterally in the direction of propagation of the wave (i.e., their contact angles decreased) while keeping their original position with respect to the IDTs. From these experiments, we conclude that ice melting and water droplet removal from the surface was more favorable for the 510 μm chip, that is, the chip operating with long wavelength Lamb waves. Some clues to account for this behavior are provided in Section 3.5, addressing the difference in the mechanical interactions of the Rayleigh SAW and Lamb AW with ice aggregates, and in Section 3.6, discussing the de-icing of large ice aggregates with these two wave types. It will be shown in Section 3.5 that interface attenuation of the 120 μm Rayleigh SAWs occurs within a distance of approximately ten wavelengths and that, therefore, the wave will initially activate the part of the ice aggregate up to a distance from the edge facing the IDT of ≈1.3 mm. This means that Rayleigh SAWs with longer wavelengths (e.g., 300 μm or higher, Table 1) would directly activate the entire ice droplet.

3.4. Active Anti-icing of Water Droplets

In real-world scenarios, avoiding ice accretion on the surfaces of substrates exposed to icing conditions is an essential function. We entitled this mode as active anti-icing to explicitly distinguish it from using anti-icing coatings extensively utilized for icephobic systems.[1–5] To test the active anti-icing capability, the chips were continuously activated with the minimum power required to prevent the transformation of water into ice under environmental conditions that otherwise induce the freezing of water droplets. It should be mentioned that the AP_T values determined in this way may be affected by inaccuracies inherent to the determination of this minimum power and that, for discussion, data should be considered only semi-quantitatively.

In the experiments, a water droplet (22 μL, at 2 °C) was delivered onto the surface of the RF-activated chips kept at the temperatures gathered in **Table 3**. Activation frequencies, incident (denoted AP_T), and effective powers are also included in this table. To estimate the active anti-icing power, various dripping trials were done with the chip excited at increasing incident powers until the water droplet remained liquid on the surface. Experiments were repeated several times to determine the reproducibility of the tests. It is important to stress the dynamic character of the experiment and that slight differences in droplet impact on the surface or surface location may affect the value of the minimum incident power required to keep the water liquid. Hence, the values of incident power in Table 3 were obtained by averaging the results for the minimum values obtained in at least three experiments where freezing was not observed. A preliminary assessment of the reported incident (i.e., AP_T) and effective power values in this table in comparison with data in Table 2 confirms that, for a given temperature, AP_T was always smaller than DP_T. The results in Table 3 also highlight that AP_T decreases when temperature increases. Significantly, it also indicates that the threshold incident power in active anti-icing experiments was always smaller for the 510 μm chip.

3.5. Simulation of AW Interaction with Small Ice Aggregates

To shed some light on the AW–ice interaction and the de-icing mechanisms on the two devices, we have simulated how the

Table 3. Active anti-icing results for the 120 and 510 μm chips: temperature, incident and effective powers, and operating frequencies.

Chip [μm][a)]	Temperature [°C]	Frequency [MHz]	Incident power AP_T [W]	Effective power [W]
120	−15	32.24	3.99 ± 0.01	2.87
	−10	32.34	2.08 ± 1.0	1.49
	−5	32.16	1.46 ± 0.32	1.05
510	−15	7.40	1.42 ± 0.13	0.98
	−10	7.39	1.29 ± 0.25	0.89
	−5	7.36	1.06 ± 0.01	0.73

[a)]All experiments were carried out for 22 μL droplets with the nozzle temperature at 2 °C. The uncertainty limits for the AP_T values define the variation in the measurements in each case.

mechanical energy of the waves is transmitted to compact droplets of ice placed on the flat surface of the LN substrate. During ice accretion processes (e.g., on the surface of airplane wings), the formation of compact glaze ice is expected at around −5 °C. However, the formation of porous rime ice is favored in ice accretion or frosting at temperatures of the order of −15 °C or lower. Herein, the finite element analysis of the AW–ice interactions has been carried out with a model reproducing the properties of glaze ice (see Section 2.4). Selected simulations at different times are reported in **Figure 5** (see videos (V6_S17 and V7_S18) of the complete series of calculated events in S17 and S18). This figure showcases a series of time-dependent snapshots of the modulus of the volumetric displacements generated both in the plate and the ice aggregate surface by the propagation of the AWs for the 120 µm R-SAW (Figure 5a) and for the 510 µm Lamb wave (Figure 5b), whose simulation was reported in Section 3.2 for the LN plate without ice. Furthermore, Figure 5c,d represent the evolution of amplitude of the surface vibrations in the outer plane of the LN plate along the wave propagation direction before and once the AWs have entered the ice–substrate interface. Similar simulation results are presented for the 510 µm R-SAW in Figure S11 and video (V8_S20), Supporting Information. At this point, it is noteworthy that the presented snapshots, plots, and videos stemming from the simulations do not aim to describe the complete melting processes of the de-icing experiments reported in Section 3.3, but to assess how efficiently and in which zone of the ice–LN interface the AW mechanical vibrations transmit their energy to the ice aggregate. In the simulations, no ice-water phase change is considered and, therefore, such simulations would not have any real physical significance whenever, in real conditions, a small amount of water starts to form at the interface or the edge of the ice aggregate due to the accumulation of energy in this zone of the ice droplet.

The snapshots in Figure 5a and the plot of the amplitude of surface oscillations in Figure 5c illustrate that the 120 µm R-SAW experiences an effective and complete damping within an

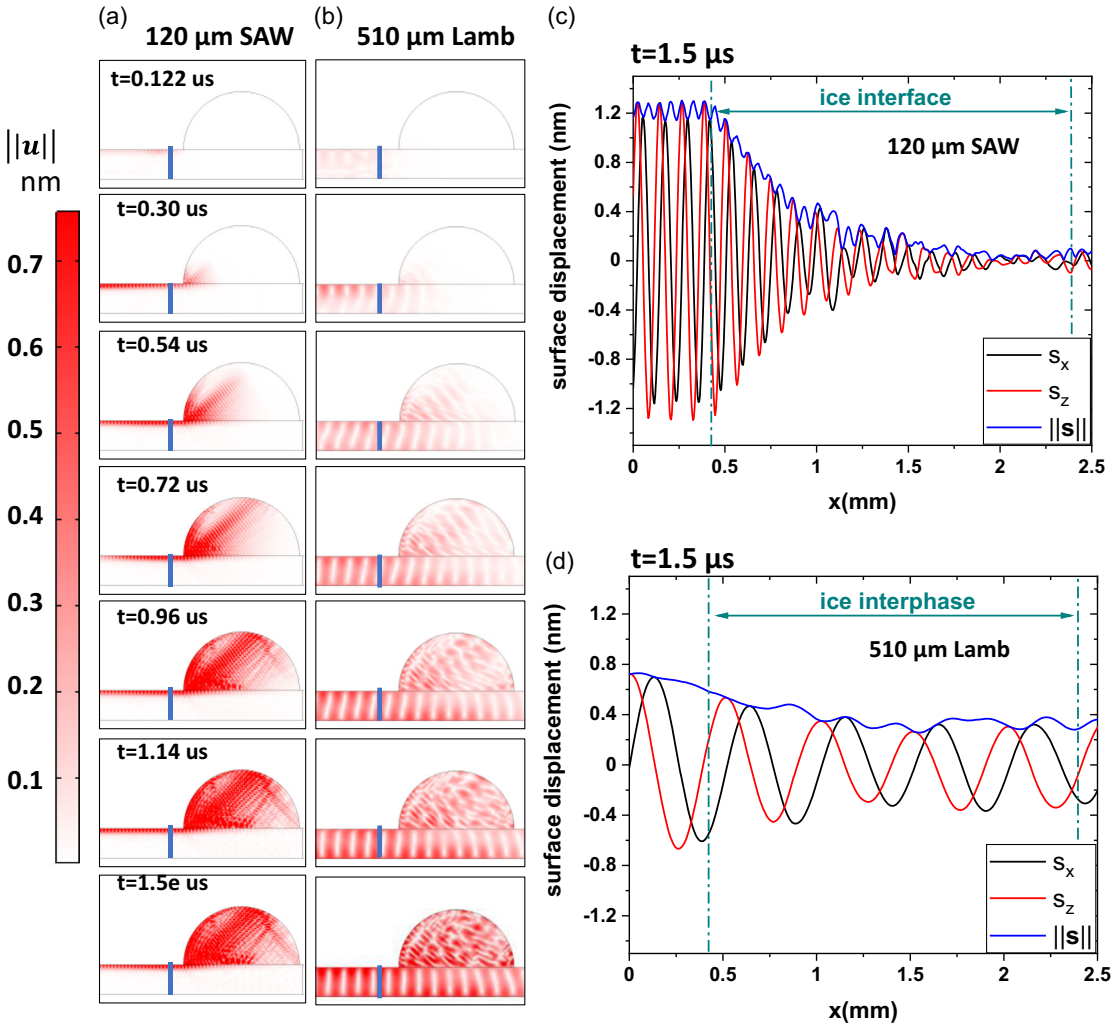

Figure 5. AW–ice interaction and surface displacements. Time-dependent simulated snapshots in the form of intensity color maps of the AW-induced displacements in the LN chips with an ice aggregate on their surface. The vertical line along the plate signals the location of the last finger of the simulated IDT. a,b) Calculations for the 120 µm SAW and 510 µm Lamb wave, correspondently. c,d) Surface displacements at the LN substrate as a function of wave propagation along the *x* coordinate direction for the 120 µm SAW (c) and 510 µm Lamb wave (d) interacting with the ice aggregate on the surface.

interface zone of ≈10–11 wavelengths (i.e., ≈1 mm). These simulations agree with previous results reported in Jacob et al.[25] Meanwhile, snapshots and plots in Figure 5b,d of the surface displacements induced by the 510 μm Lamb wave in Figure 5b,d reveal that the amplitude of the wave is less affected in this case (i.e., damping is less effective) by the interaction with ice, and therefore, the wave is not fully attenuated within the surface zone covered by the ice droplet. This means that Lamb waves can propagate their energy along larger zones of the ice-substrate interface than R-SAW.

Of particular relevance is the comparison of the 510 μm Lamb wave with the simulations done for the 510 μm R-SAW (see Figure S11, Supporting Information). It is apparent from this comparison that although the latter can effectively traverse through the entire ice-substrate interface without experiencing complete damping, the attenuation percentage after crossing the ice droplet is in the order of 75% for the 510 μm R-SAW and just 35% for the 510 μm Lamb wave. Although this simulation analysis must be taken as preliminary and should be complemented with experimental evidences, it suggests that both wavelength and type of wave are essential characteristics affecting the AW-ice interaction.

The assessment of experimental data for the melting of water droplets reported in the previous section and the commented features from the simulations in the present section permit advancing some specific considerations about the de-icing mechanism: 1) Simulations show that the 120 μm R-SAW is effectively damped when penetrating the ice-substrate interface, and its intensity almost decreases to zero at about half the substrate length covered by the small ice aggregate (Figure 5a,c). In other words, most energy carried by the AWs is effectively delivered to the ice within a short distance inside the ice edge zone in front of the IDTs. Under these conditions, it is the most likely that in the experiment the side of the droplet facing the IDT will be converted into water. Once water starts to form, the physical model in Figure 5a loses the experimental meaning because it does not represent the mixture water/ice existing in the experiments and the fact that once water is formed, the transmission of mechanical energy from the R-SAW to the liquid phase will be more favorable than to solid ice (i.e., damping would be even more effective). This situation was already highlighted in our previous work describing the ice melting mechanism induced by R-SAW, where we proposed that once a first portion of liquid water forms on the side of the ice aggregate facing the R-SAW propagation front, a water heat streaming mechanism is the main responsible for de-icing;[25] and 2) Simulations show that the Lamb wave generated in the 510 μm chip is less damped along the ice-substrate interface and penetrates long distances along the surface covered with ice (Figure 5c,d). It is interesting to highlight that the simulations showcase that only some but not complete damping occurs within the ice-substrate interface for the small ice aggregate used for the simulations and the experiments in Section 3.3. This limited damping enables that the whole ice-substrate interface of the ice aggregate is affected by the AW activation. Since the transmitted mechanical energy is not very high, the wave is expected to initially provoke ice cracking and surface softening along the entire ice-substrate interface before that extensive melting takes place in a second instance. The next section provides additional experimental evidence of this mechanism. This analysis and the previous comparison in Figure S11, Supporting Information between the simulations for the 510 μm R-SAW and 510 μm Lamb waves also support that both wavelength and type of wave (R-SAW or Lamb waves) are factors modulating the interaction mechanism between ice aggregates and AWs.

3.6. Proof-of-Concept De-Icing of Large Ice Aggregates and Layers. De-Icing Mechanism

From the previous analysis and simulations, some key features can be deduced regarding the de-icing mechanism of small droplets: 1) longer wavelength seems more efficient for ice melting (for the given droplet size); 2) melting with a traveling R-SAW is rather directional from one droplet side to the other and proceeds first in the edge facing the IDTs; and 3) melting with a long wavelength Lamb wave is less directional due to a lower attenuation by the droplet and the reflection of the wave on the free side of the plate.

In a leap forward, to further characterize the specificities in the de-icing mechanisms using Lamb waves, we present in this section two proof-of-concept de-icing experiments of large ice aggregates. Experiments were conducted with 510 μm Lamb waves and two different chip configurations. The purpose is to approach the situation encountered in real-world icing processes, where large amounts of ice will cover most or all of the activated substrate area,. For comparison, a similar de-icing experiment of a big ice aggregate was carried out with a 420 μm chip generating Rayleigh SAW waves with a wavelength close to that of the 510 μm chip generating Lamb waves.

In Experiment 1 (see a detailed description in the Methods section), an ice layer with a thickness estimated between 0.5- and 1 mm became accreted in an open IWT at −10 °C, conditions favoring the formation of mixed ice and some incipient porosity.[35,40] AW de-icing was then activated in a cool room at −10 °C. Purposely, the ice was accreted on the LN surface opposite to the IDTs. The IDTs we prepared in the center of the LN chip with the connected pads emplaced at the two sides as indicated in Figure S5, Supporting Information (note that the pad at the top was the one electrically activated, while that at the bottom was grounded). This experimental configuration is intended to prove two features: first, that Lamb wave oscillations extend through the whole piezoelectric plate and, second, that these waves can induce de-icing on the surface opposite to the surface with IDTs (i.e., to prove that Lamb waves are effective on the two sides of the plate). A scheme of the experimental setup is reported as an insert in **Figure 6**a. The evolution of the de-icing process in this experiment can be discussed following the series of snapshot photographs reported in this figure (see the original video (V9_S21) in the SI). The first evidence is that chip activation enabled the effective removal of the ice accreted on the side opposite the IDTs and that the surface became free from ice. This proved that lattice oscillations extending through the whole thickness of the plate bear enough power to activate the de-icing process. Deicing took ≈98 s from the application of the RF signal (snapshot a1) up to the end of the process (snapshot a7). Interestingly, de-icing involved a first step (snapshots a2/a3) where ice cracking extended along the whole surface in about 10–12 s, from $t = 36$ s to $t = 48$ s. Melting occurred as a second step and took much longer than the initial cracking (about 50 s)

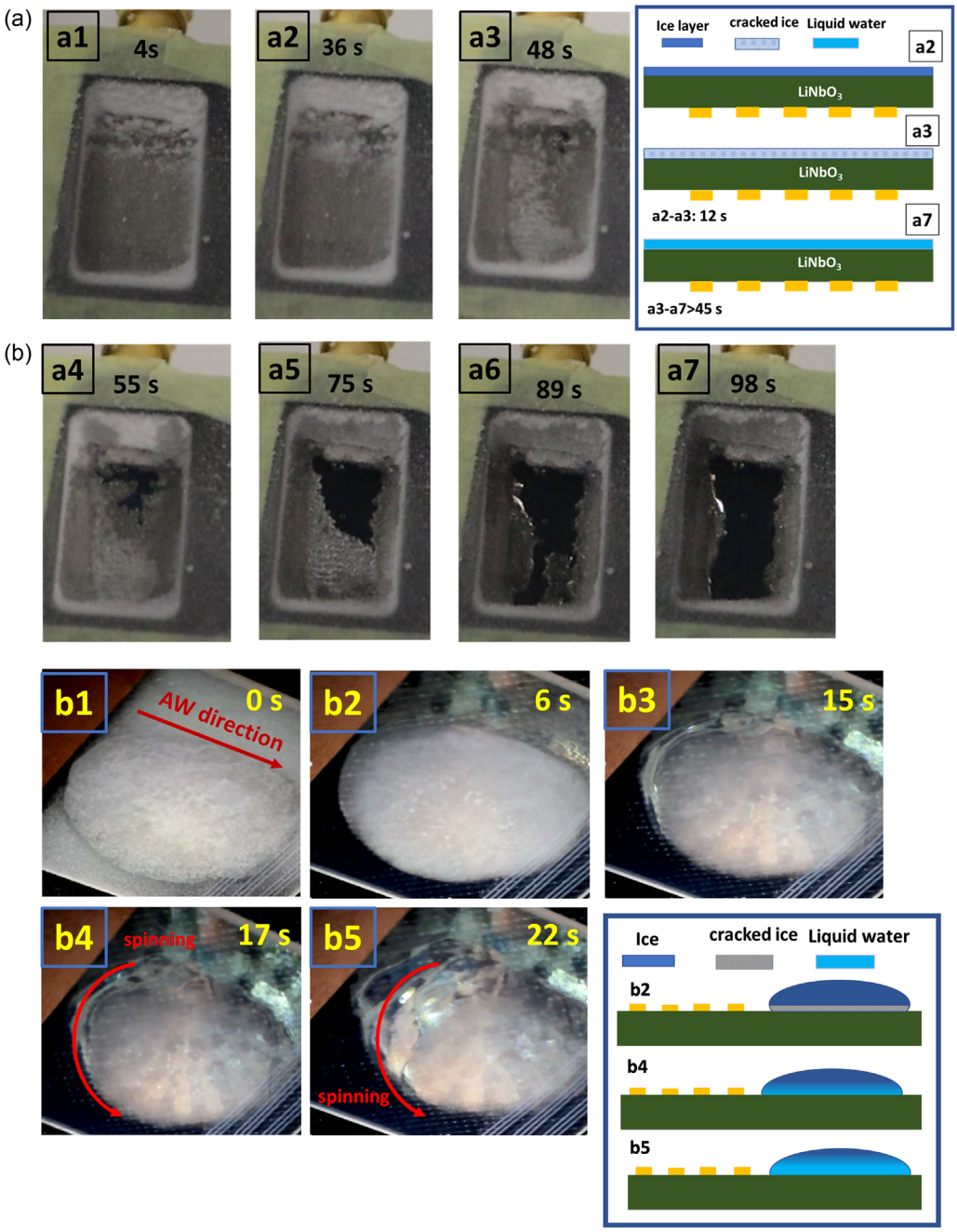

Figure 6. Proof-of-concept experiments: Experiment 1: a) Snapshot of a de-icing experiment induced with the 510 µm chip activated at 7.3 MHz with the IDTs at the back side of the LN chip as shown in Figure S5c and S5d, Supporting Information; a1) Initial state with 1 mm of ice accreted on the surface of the chip; a2) Initial formation of cracks atop the IDT; a3) crack region extends to cover the whole chip in the direction of AW propagation; a4–a7) melting of ice on the zone atop the IDT. Inset: schematic of the de-icing mechanism induced by long-wavelength Lamb waves. Experiment 2: b) Snapshots of a de-icing experiment induced with the 510 µm chip activated at 7.3 MHz and a big ice aggregate facing the IDTs placed on the same side: b1) application of the AW; b2) ice change aspect without changes in the perimeter. Frost around disappears; b3) Progression of activation: some water forms at the edge facing the IDTs; b4,b5) melting occurs in the whole aggregate, and water and ice coexist in the melted zones. The circular arrows in (b4,b5) signal the direction of rotation of the floating ice particle the images around these two snapshots. Inset: schematic of the de-icing mechanism induced by long-wavelength Lamb waves.

from $t = 48$ s to $t = 98$ s. At the end of the melting process, the on-chip temperature was 10 °C, while in the close vicinity of the chip, the temperature remained at −8 °C.

For clarity, the aforementioned de-icing steps are illustrated with a cartoon in the schematic included in Figure 6. We hypothesize that the initial cracking step in Schematic a3 is induced by

the interaction of the ice layer with the activated substrate through the exchange of mechanical energy. The subsequent melting process in schematic a7 will mainly involve heating by acoustic-thermal effects and possibly some heat from the Joule effect due to ohmic losses at the IDTs beneath. The downward direction of this melting process is likely the result of some preferential heating at the side where the electrically active pole is connected to one of the pads.

In Experiment 2, a larger aggregate of ice at −15 °C is placed on the same surface-side as the IDTs. Since the ice did not form by accretion but by cooling a big droplet of previously deposited water, no significant porosity is expected, even if grown at this low temperature. The de-icing process took place according to a series of steps characterized by the snapshots in Figure 6b (the video (V10_S22) of the entire process is reported in the SI section S22) and illustrated by the schematics inserted in this figure. It is apparent that after 15 s of activation, the frost accumulated around the big aggregate of ice during the manipulation of the probe device disappeared. At this stage, the profile shape of the big aggregate of ice was not altered, although changes in its aspect (brightness and whiteness of the aggregate) suggest that the interface with the substrate might be affected. Changes were more profound after 19 and 22 s (snapshots b4/b5) of excitation when a mixture of ice/water coexists in the whole volume and the big ice particle still existing in the center spins as it is signaled with an arrow in these snapshots and can be directly appreciated in the video (V10_S22), Supporting Information. A significant feature of this experiment is that no defined lateral water/ice front formed during AW excitation.

For comparison, a similar de-icing experiment of a big ice aggregate was carried out with a 420 μm chip generating Rayleigh SAW waves. A video (V11_S23) of the de-icing process is shown in supporting information S23. This video (V11_S23) and the selected snapshots reported in Figure S12, Supporting Information of the supporting information show that the de-icing process begins at the edge of the aggregate facing the IDTs and that melting progresses from this side, where a zone of ≈4–5 mm wide converts readily into water, to the other side of the ice aggregate. This phenomenology of de-icing is typical of a mechanism induced by Rayleigh SAW and coincides with previous studies on this type of process.[25]

Interestingly, the sequence cracking/melting extended along the whole interface found in Experiment 1 and the intermixing of ice-water in Experiment 2 strongly differ from the de-icing phenomenology found for de-icing large aggregates of compact ice when excitation is induced with R-SAWs (see video (V11_S23) and Figure S12, Supporting Information) on poorly heat conducting substrates.[25] In that case, no extensive cracking was detected, and de-icing followed a lateral progression of a well-defined water-ice front, which, starting at the side facing the IDT, progressed until the completion of the melting process. A similar waterfront-ice interaction has also been claimed for SAW de-icing of highly porous rime ice formed by frosting.[30] The experimental findings in Figure 6 showcase that de-icing of large ice aggregates with Lamb waves occurs through a different mechanism, which can be summarized in the following two steps: 1) ice cracking along a large zone of the ice–substrate interface; 2) progressive melting along the affected area, a process where ice and liquid water may appear mixed in the excited zones.

The simulations of the power injection of 120 μm R-SAWs into the ice have shown that this process is restricted to a small region of the interface (c.f., Figure 5c). Once the water is formed in this zone, the progression of de-icing will depend on the efficiency of heat transmission through the lateral water–ice interface, a process whose efficiency would be limited by the small area of such interface available for heat diffusion and likely diminished by heat losses from the water zone into the air. Meanwhile, since the power coupling between the 510 μm Lamb wave and ice is less intense, the wave may affect a much larger ice–substrate interface (c.f., Figure 5d). Since the transmitted mechanical energy is insufficient to induce a rapid melting, in Experiment 1 ice cracking has been found to be the first step of the de-icing process. Then, the heat caused by acoustothermal effects due to the electrical activation of the device would be transmitted through the entire cracked ice/substrate interface without losses into the air. Paradoxically, the less intense LN-ice AW mechanical coupling found for the 510 μm Lamb wave appears to render a more efficient de-icing process, at least for small ice aggregates, as indicated by the data in Table 2 and 3. Further advances in this evaluation of results would require additional analysis of heat transmission through the different interfaces involved in the examined systems, a question that remains open for future investigations.

4. Conclusions

The experiments and simulations in this work have disclosed the different de-icing mechanisms intervening during the interaction with ice of traveling AWs generated in piezoelectric substrates. It has also been determined that the de-icing efficiency, at least to melt small ice aggregates, is highly dependent on the characteristics of the AW used in each case. In particular, through the analysis and simulation of the interaction with ice of an R-SAW of relatively short wavelength and that of a long wavelength Lamb wave, significant differences have been found in the phenomenology of de-icing for each type of these waves. Thus, it has been shown that R-SAW effectively transmits to ice most of its mechanical energy within a small area of the interface, while Lamb waves with comparatively longer wavelengths are less damped and may transit through a longer distance of the ice–substrate interface without experiencing a strong attenuation. Regarding the de-icing process, these specific properties of the AW-ice mechanical interactions lead, as a first step, to the direct melting of the ice edge when the activation is done with R-SAWs but to ice cracking within a large interface area when the activation is done with long wavelength Lamb waves. Progression of a water–ice front and interface melting over a large area are the successive steps of the de-icing process induced by these two types of AWs. Both kinds of AW and their distinct wavelengths seem to be essential features responsible for these differences. For the conditions explored in the present work, this combination of factors rendered that de-icing and active anti-icing were more favorable with Lamb waves. Additional studies should be carried out to quantitatively determine the influence of each of these two characteristics.

This first approach to determining the factors that control the mechanisms of de-icing induced by Rayleigh waves and long

wavelength Lamb waves has been possible through combining experiments with $LiNbO_3$ model systems and the finite element simulation of the AW–ice interaction. In this regard, results and simulations should be considered as a first step in investigating the use of AWs to prevent icing. Extrapolation of the findings reported here to other experimental conditions, different supports, types of waves, and icing conditions is not automatic, and specific experiments/simulations would be necessary to account for the phenomenology encountered in each case. In this regard, we deem that wavelength, type of wave (e.g., Lamb or Rayleigh, a different kind of surface waves or thickness shear waves), traveling or stationary waves, state of the surface, tilting angles of the substrates, etc., are critical characteristics that should be considered explicitly for a proper evaluation of de-icing mechanism and efficiencies.

Supporting Information

Supporting Information is available from the Wiley Online Library or from the author.

Acknowledgements

The authors thank the projects PID2022-143120OB-I00 and TED2021-130916B-I00 funded by MCIN/AEI/10.13039/501100011033 and by "ERDF (FEDER)" A way of making Europe, Fondos NextgenerationEU and Plan de Recuperación, Transformación y Resiliencia". CLS thanks the University of Seville through the VI PPIT-US and "Ramon y Cajal" program funded by MCIN/AEI/10.13039/501100011033. This research work is funded by the EU H2020 program under grant agreement 899352 (FETOPEN-01-2018-2019-2020 – SOUNDofICE).

Conflict of Interest

The authors declare no conflict of interest.

Author Contributions

Shilpi Pandey: conceptualization (equal); data curation (equal); formal analysis (equal); investigation (equal); methodology (equal); writing—original draft (equal). **Jaime del Moral**: data curation (equal); formal analysis (equal); investigation (equal); methodology (equal); writing—review & editing (equal). **Stefan Jacob**: data curation (supporting); formal analysis (supporting); investigation (supporting); methodology (supporting); writing—review & editing (supporting). **Laura Montes**: investigation (supporting); methodology (supporting); writing—review & editing (supporting). **Jorge Gil-Rostra**: investigation (supporting); methodology (supporting); writing—review & editing (supporting). **Alejandro Frechilla**: investigation (supporting); methodology (supporting); writing—review & editing (supporting). **Atefeh Karimzadeh**: investigation (supporting); methodology (supporting); writing—review & editing (supporting). **Victor J. Rico**: investigation (supporting); methodology (supporting); writing—review & editing (supporting). **Raul Kanter**: investigation (supporting); methodology (supporting); writing—review & editing (supporting). **Niklas Kandelin**: investigation (supporting); methodology (supporting); writing—review & editing (supporting). **Carmen López-Santos**: investigation (supporting); methodology (supporting); writing—review & editing (supporting). **Heli Koivuluoto**: funding acquisition (supporting); investigation (supporting); methodology (supporting); writing—review & editing (supporting). **Luis Angurel**: funding acquisition (supporting); investigation (supporting); methodology (supporting); writing—review & editing (supporting). **Andreas Winkler**: funding acquisition (supporting); investigation (supporting); methodology (supporting); writing—review & editing (supporting). **Ana Borrás**: conceptualization (equal); formal analysis (equal); funding acquisition (lead); investigation (equal); methodology (equal); supervision (equal); writing—original draft (equal). **Agustin R. González-Elipe**: conceptualization (equal); formal analysis (equal); funding acquisition (supporting); investigation (equal); methodology (equal); supervision (equal); writing—original draft (equal).

Data Availability Statement

The data that support the findings of this study are available from the corresponding author upon reasonable request.

Keywords

acoustic waves, active anti-icing, de-icing, ice melting, Lamb wave, Rayleigh surface wave, wavelength

Received: August 1, 2024
Revised: October 21, 2024
Published online:

[1] G. Peng, Y. Zheng, M. Wen, C. Song, Y. Lin, L. Jiang, *Adv. Mater.* **2012**, *19*, 2642.
[2] M. I. Jamil, A. Ali, F. Haq, Q. Zhang, X. Zhan, F. Chen, *Langmuir* **2018**, *34*, 15425.
[3] K. Golovin, S. P. R. Kobaku, D. H. Lee, E. T. DiLoreto, J. M. Mabry, A. Tuteja, *Sci. Adv.* **2016**, *2*, e1501496.
[4] V. Rico, J. Mora, P. Garcia, A. Borras, A. R. Gonzalez-Elipe, C. Lopez-Santos, *Appl. Mater. Today* **2020**, *21*, 100815.
[5] M. J. Wood, G. Brock, J. Debray, P. Servio, A. M. Kietzig, *ACS Appl. Mater. Interfaces* **2022**, *14*, 47310.
[6] H. Memon, J. Wang, X. Hou, *Materials* **2023**, *16*, 4607.
[7] J. Zheng, R. Liu, D. Liu, Z. Weng, G. Song, W. Li, Z. Wang, *Prog. Org. Coat.* **2012**, *175*, 107308.
[8] Z. Zhu, H. Liang, D.-W. Sun, *ACS Appl. Mater. Interfaces* **2023**, *15*, 14874.
[9] L. B. Boinovich, E. V. Chulkova, K. A. Emelyanenko, A. G. Domantovsky, A. M. Emelyanenko, *J. Colloid Interface Sci.* **2022**, *609*, 260.
[10] L. Li, S. Khodakarami, X. Yan, K. F. Rabbi, A. A. Gunay, A. Stillwell, N. Miljkovic, *Adv. Funct. Mater.* **2022**, *32*, 2201521.
[11] O. Redondo, S. G. Prolongo, M. Campo, C. Sbarufatti, M. Giglio, *Compos. Sci. Technol.* **2018**, *164*, 65.
[12] A. A. Muhsan, K. Lafdi, *Mater. Today: Proc.* **2022**, *52*, 206.
[13] N. Karim, M. Zhang, S. Afroj, V. Koncherry, P. Potluri, K. S. Novoselov, *RSC Adv.* **2018**, *8*, 16815.
[14] N. Li, Y. Zhang, H. Zhi, J. Tang, Y. Shao, L. Yang, T. Sun, H. Liu, G. Xue, *Chem. Eng. J.* **2022**, *429*, 132183.
[15] Y. Li, W. Ma, Y. S. Kwon, W. Li, S. Yao, *Adv. Funct. Mater.* **2022**, *32*, 2113297.
[16] X. Fang, Y. Liu, S. Lei, C. Li, J. Ou, A. Amirfaz, *RSC Adv.* **2022**, *12*, 13792.
[17] X. Yin, Y. Zhang, D. Wang, Z. Liu, Y. Liu, X. Pei, B. Yu, F. Zhou, *Adv. Funct. Mater.* **2015**, *25*, 4237.
[18] H. Zhang, X. Xu, M. Wu, Y. Zhao, F. Sun, Q. Xin, Y. Zhou, M. Qin, Y. Zhou, C. Ding, J. Li, *Adv. Funct. Mater.* **2022**, *32*, 2201795.
[19] V. Daniliuk, Y. Xu, R. Liu, T. He, X. Wang, *Renewable Energy* **2020**, *145*, 2005.
[20] Y. Li, H. Shen, W. Guo, *Energies* **2021**, *14*, 8246.
[21] D. Yang, R. Tao, X. Hou, H. Torun, G. Mchale, J. Martin, Y. Q. Fu, *Adv. Mater. Interfaces* **2021**, *8*, 2001776.

[22] X. Zeng, H. Ong, L. Haworth, Y. Lu, D. Yang, M. Rahmati, Q. Wu, H. Torun, J. Martin, X. Hou, X. Lv, W. Yuan, Y. He, Y. Fu, *ACS Appl. Mater. Interfaces* **2023**, *15*, 35648.
[23] X. Zeng, Z. Yan, Y. Lu, Y. Fu, X. Lv, W. Yuan, Y. He, *Langmuir* **2021**, *37*, 11851.
[24] J. del Moral, L. Montes, V. Rico-Gavira, C. López-Santos, S. Jacob, M. Oliva-Ramirez, J. Gil-Rostra, A. Fakhfouri, S. Pandey, M. Gonzalez del Val, J. Mora, P. García-Gallego, P. F. Ibáñez-Ibáñez, M. A. Rodríguez-Valverde, A. Winkler, A. Borrás, A. R. González-Elipe, *Adv. Funct. Mater.* **2023**, *33*, 2209421.
[25] S. Jacob, S. Pandey, J. Del Moral, A. Karimzadeh, J. Gil-Rostra, A. R. González-Elipe, A. Borrás, A. Winkler, *Adv. Mater. Technol.* **2023**, *8*, 2300263.
[26] A. Karimzadeh, U. Weissker, J. del Moral, A. Winkler, A. Borrás, A. R. González-Elipe, S. Jacob, *Adv. Mater. Technol.* **2024**, *9*, 2301749.
[27] V. I. Anisimkin, N. V. Voronova, *Ultrasonics* **2021**, *116*, 106496.
[28] P. Schulmeyer, M. Weihnacht, H. Schmidt, *Sensors* **2024**, *24*, 2292.
[29] V. Anisimkin, V. Kolesov, A. Kuznetsova, E. Shamsutdinova, I. Kuznetsova, *Sensors* **2021**, *21*, 919.
[30] D. Yang, L. Haworth, P. Agrawal, R. Tao, G. McHale, H. Torun, J. Martin, J. Luo, X. Hou, Y. Fu, *Langmuir* **2022**, *38*, 11314.
[31] M. Rashedul, H. Sarker, J. L. Silva, M. Castaneda, B. Wilburn, Y. Lin, N. Love, *J. Intell. Mater. Syst. Struct.* **2018**, *29*, 938.
[32] C. Zhaoa, W. Genga, X. Qiaoa, F. Xuea, J. Hea, G. Xuea, Y. Liua, H. Weia, K. Bia, Y. Lib, M. Xunb, X. Choua, *Sens. Actuators: A Phys.* **2022**, *333*, 113230.
[33] H. Lu, Y. Li, J. Zhang, *Sensors* **2021**, *21*, 3672.
[34] A. Winkler, S. Menzel, H. Schmidt, in *Proc. of SPIE*, vol. *7362*, SPIE Europe Microtechnologies for the New Millennium, Dresden, Germany **2009**, p. 73621Q.
[35] G. Fortin, J. Perron, in *47th AIAA Aerospace Sciences Meeting Including The New Horizons Forum and Aerospace Exposition*, Orlando, FL, January **2009**, p. AIAA 2009-0274.
[36] H. Koivuluoto, C. Stenroos, R. Ruohomaa, G. Bolelli, L. Lusvarghi, P. Vuoristo, in *Proc. of the Int. Workshop on Atmospheric Icing of Structures (IWAIS)*, Uppsala, Sweden **2015**, p. 28.
[37] A. Fakhfouri, C. Devendran, T. Albrecht, D. Collins, A. Winkler, H. Schmidt, A. Neild, *Lab Chip* **2018**, *18*, 2224.
[38] D. Mandal, S. Banerjee, *Sensors* **2022**, *22*, 820.
[39] G. Kovacs, M. Anhorn, H. E. Engan, G. Visintini, C. C. W. Ruppel, *IEEE Symp. Ultrason.* **1990**, *1*, 438.
[40] V. F. Petrenko, R. W. Whitworth, in *Physics of Ice*, Oxford University Press, Oxford **2002**.
[41] Perfectly Matched Layers, https://doc.comsol.com/5.5/doc/com.comsol.help.aco/aco_ug_pressure.05.106.html (accessed: July 2024).
[42] E. A. Ash, in *Acoustic Surface Waves* (Ed: A. A. Oliner), Springer, Berlin **1978**.
[43] P. Brunet, M. Baudoin, O. Bou Matar, F. Zoueshtiag, *Phys. Rev. E* **2010**, *81*, 036315.
[44] A. Wixforth, C. Strobl, C. Gauer, A. Toegl, E. J. Scriba, Z. V. Guttenberg, *Anal. Bioanal. Chem.* **2004**, *379*, 982.
[45] R. J. Shilton, V. Mattoli, M. Travagliati, M. Agostini, A. Desii, F. Beltram, M. Cecchini, *Adv. Funct. Mater.* **2015**, *25*, 5895.
[46] H. L. Ong, D. Yang, H. Chen, J. Zhou, L. Haworth, J. Zhang, D. Gibson, P. Agrawal, H. Torun, Q. Wu, X. Hou, *Mater. Chem. Phys.* **2023**, *304*, 127842.
[47] M. Baudoin, R. Chutani, F. Bretagnol, A. Peret, US 20240042969A1 **2024**, https://patents.google.com/patent/US20240042969A1/en?oq=.+US+2024%2f0042969+A1.